

Non-equilibrium hydrodynamics of a rotating filament

H. WADA and R. R. NETZ

Physik Department, Technical University Munich, 85748 Garching, Germany

PACS. 87.15.-v – Biomolecules: structure and physical properties.

PACS. 47.20.Ky – Nonlinearity, bifurcation, and symmetry breaking.

PACS. 47.63.mf – Low-Reynolds-number motion.

Abstract. – The nonlinear dynamics of an elastic filament that is forced to rotate at its base is studied by hydrodynamic simulation techniques; coupling between stretch, bend, twist elasticity and thermal fluctuations is included. The twirling-overwhirling transition is located and found to be strongly discontinuous. For finite bend and twist persistence length, thermal fluctuations lower the threshold rotational frequency, for infinite persistence length the threshold agrees with previous analytical predictions.

The dynamics and morphology of elastic filaments are of interest in various fields encompassing systems on many different length scales [1]. Relevant examples are provided by biopolymers and bio-assemblies, including DNA, actin filaments, microtubules, and multicellular organisms like *Bacillus subtilis* [2]. Modern micro-manipulation techniques allow to observe and analyze filament dynamics on the single-molecule level [3], prompting a detailed understanding of the combined effects of fluctuations, hydrodynamics and elasticity. Static properties of elastic rods under external force loads have a long history of study, dating back to Euler [4]. Of current interest is the time-dependent behavior of such driven filaments and the possibility of shape bifurcations, especially on the biologically relevant nano-to-micro length scales, where viscous hydrodynamic dissipation dominates over inertia.

In this Letter, we describe a hydrodynamic simulation technique for elastic filaments with arbitrary shape and rigidity and subject to external forces or boundary conditions, including full coupling between thermal, elastic and hydrodynamic forces in low-Reynolds-number flow. We apply our method to the whirling dynamics of a slender filament that is axially rotated at one end at frequency ω (while the other end is free). This model system has first been studied analytically by Wolgemuth *et al.* [5], who showed that a critical frequency ω_c separates whirling (steady-state crankshafting motion with axial spinning) from twirling (diffusion-dominated simple axial rotation) by a supercritical Hopf bifurcation (i.e., a continuous shape transition). Subsequently, a zero-temperature simulation has been performed using the immersed boundary method [6], where the microscopic structure of the filament was modelled by interconnected springs. In contrast to analytic predictions, the filament was shown to undergo a subcritical (i.e. discontinuous) shape transition from twirling to a strongly bent state where the filament almost folds back on itself (termed *overwhirling*). The transition frequency ω_c was found to be smaller by a factor of 3.5 compared to the analytic estimate. Using our simulation technique, we first map out the stability diagram in the absence

of thermal fluctuations as a function of the driving rotational frequency; ω_c is identified as the instability point of twirling and agrees quantitatively with analytical prediction [5]; however, a stable small-amplitude whirling state is absent and instead a strongly bent overwhirling state is found for all frequencies ω larger than ω_c . In the presence of thermal fluctuations the transition frequency ω^* decreases as the filament becomes more flexible and the discontinuous nature of the transitions is manifested by pronounced hysteresis.

To proceed, consider a filament with circular cross section and contour length L , parameterized by arclength s . A generalized Frenet orthonormal basis $\{\hat{\mathbf{e}}_1, \hat{\mathbf{e}}_2, \hat{\mathbf{e}}_3\}$ is defined at each point of the filament centerline $\mathbf{r}(s)$, where $\hat{\mathbf{e}}_3$ points along the tangent and $\hat{\mathbf{e}}_1, \hat{\mathbf{e}}_2$ lie in the plane normal to $\hat{\mathbf{e}}_3$ such that the basis forms a right-handed triad, i.e. $\hat{\mathbf{e}}_2 = \hat{\mathbf{e}}_3 \times \hat{\mathbf{e}}_1$. The strain vector $\boldsymbol{\Omega}(s) = (\Omega_1, \Omega_2, \Omega_3)$ characterizes the shape of the filament through the kinematic relation $\partial_s \hat{\mathbf{e}}_j = \boldsymbol{\Omega} \times \hat{\mathbf{e}}_j$, where $\kappa = (\Omega_1^2 + \Omega_2^2)^{1/2}$ is the curvature and Ω_3 the twist density. The elastic energy of an elastic inextensible rod reads [4]

$$E = \frac{A}{2} \int_0^L ds [(\Delta\Omega_1)^2 + (\Delta\Omega_2)^2] + \frac{C}{2} \int_0^L ds (\Delta\Omega_3)^2, \quad (1)$$

where A and C are bend and twist rigidity constants, and $\Delta\boldsymbol{\Omega} = \boldsymbol{\Omega} - \boldsymbol{\Omega}^0$. The ground state shape of the filament is thus controlled by the intrinsic curvatures Ω_1^0, Ω_2^0 and the intrinsic twist Ω_3^0 . According to the principle of virtual work, the force per length acting on the filament is obtained via $\mathbf{f} = -\delta E / \delta \mathbf{r}$ keeping the rotation angle about the tangent zero, i.e., $\delta\phi = \hat{\mathbf{e}}_2 \cdot \delta\hat{\mathbf{e}}_1 = 0$ [7]. Likewise the torque about the tangent is obtained via $m = -\delta E / \delta\phi$ without moving the centerline, i.e., $\delta\mathbf{r} = 0$. In the low-Reynolds-number limit, the local force and torque balance with the viscous drag (long-range hydrodynamic interaction will be considered later), leading to the equations $\dot{\mathbf{r}} = \mu\mathbf{f}$ and $\dot{\phi} = \mu_r m$, where $\dot{\mathbf{r}} = \partial\mathbf{r}/\partial t$ and μ, μ_r are the translational and rotational mobility constants.

For an efficient simulation code, it is crucial to introduce a laboratory-fixed reference frame $\{\hat{\mathbf{x}}, \hat{\mathbf{y}}, \hat{\mathbf{z}}\}$ and to parameterize $\boldsymbol{\Omega}$ (thereby the energy E) in terms of \mathbf{r} [8]. The unit vector $\hat{\mathbf{n}} = \mathbf{t} \times \hat{\mathbf{z}} / |\mathbf{t} \times \hat{\mathbf{z}}|$ is by construction normal to the tangent $\mathbf{t} \equiv \hat{\mathbf{e}}_3$. Taking the binormal $\mathbf{b} = \mathbf{t} \times \mathbf{n}$, we find a local right-handed triad $\{\mathbf{n}, \mathbf{b}, \mathbf{t}\}$ at the filament centerline position $\mathbf{r}(s)$. Since $(\hat{\mathbf{e}}_1, \hat{\mathbf{e}}_2)$ and (\mathbf{n}, \mathbf{b}) are coplanar by definition, they are related as $\hat{\mathbf{e}}_1 + i\hat{\mathbf{e}}_2 = \exp[-i\theta(s)](\mathbf{n} + i\mathbf{b})$. The rotation angle about the tangent thus satisfies $\delta\phi = \delta\theta + \mathbf{b} \cdot \delta\mathbf{n}$, indicating that \mathbf{r} and θ are not independent in computing the translational force \mathbf{f} . Using the kinematic relation $\Omega_1 = -\hat{\mathbf{e}}_2 \cdot \partial_s \hat{\mathbf{e}}_3$, $\Omega_2 = \hat{\mathbf{e}}_1 \cdot \partial_s \hat{\mathbf{e}}_3$, and $\Omega_3 = \hat{\mathbf{e}}_2 \cdot \partial_s \hat{\mathbf{e}}_1$, it is straightforward to express (1) in terms of \mathbf{r} and θ .

In our dynamic simulation, the filament is modelled as a chain of $N+1$ connected spheres of diameter a . Each bead is specified by its position \mathbf{r}_j and the twist angle with respect to the laboratory frame, θ_j , from which the strain vector $\boldsymbol{\Omega}_j$ is calculated at each sphere point. The unit tangent is thus given by $\mathbf{t}_j = \mathbf{u}_j / |\mathbf{u}_j|$, where $\mathbf{u}_j = \mathbf{r}_{j+1} - \mathbf{r}_j$ is the bond vector. The simplest symmetric discretization of Ω_3 is by $\Omega_{3,j} = [\frac{1}{2}(\mathbf{e}_2 \cdot \partial_s \mathbf{e}_1 - \mathbf{e}_1 \cdot \partial_s \mathbf{e}_2)]_j = f_j \sin(\theta_j - \theta_{j-1}) + g_j \cos(\theta_j - \theta_{j-1})$, where f and g are functions of $\{\mathbf{r}_j\}$ only. The total elastic energy E involves the stretching contribution: $E_{tot} = E[\mathbf{r}, \theta] + \sum_{j=1}^{N-1} K / (2a)(|\mathbf{u}_j| - a)^2$. For an isotropic rod, the stretching modulus K is given by $K = 16A/a^2$. Writing the angular velocity as $\partial_t \phi = \partial_t \theta + \mathbf{b} \cdot \partial_t \mathbf{n}$ and using $\nabla_{\mathbf{r}_j} \theta = -\mathbf{b} \cdot \nabla_{\mathbf{r}_j} \mathbf{n}$, we arrive at the coupled Langevin equations

$$\dot{\mathbf{r}}_i(t) = \sum_{j=1}^{N+1} \boldsymbol{\mu}_{ij}(\mathbf{r}_{ij}) \left[-\nabla_{\mathbf{r}_j} E_{tot}|_{\theta} + \sum_{k=1}^{N+1} \nabla_{\theta_k} E_{tot}|_{\mathbf{r}} \mathbf{b}_k \cdot \nabla_{\mathbf{r}_j} \mathbf{n}_k \right] + \boldsymbol{\xi}_i(t), \quad (2)$$

$$\dot{\theta}_i(t) = -\mathbf{b}_i \cdot \dot{\mathbf{n}}_i - \mu_r \nabla_{\theta_j} E_{tot} + \Xi_i(t). \quad (3)$$

Hydrodynamic interactions between two spheres i and j are included via the Rotne-Prager mobility tensor $\boldsymbol{\mu}_{ij}(\mathbf{r}_{ij}) = 1/(8\pi\eta r_{ij})[\mathbf{1} + \hat{\mathbf{r}}_{ij}\hat{\mathbf{r}}_{ij} + a^2/(2r_{ij}^2)(\mathbf{1}/3 - \hat{\mathbf{r}}_{ij}\hat{\mathbf{r}}_{ij})]$, where $\hat{\mathbf{r}}_{ij} = \mathbf{r}_{ij}/r_{ij}$ and η the solvent viscosity [9]. For the translational and rotational self-mobilities of the spherical monomers with diameter a we use $\boldsymbol{\mu}_{ii} = \mathbf{1}/(3\pi\eta a) \equiv \mu_0\mathbf{1}$ and $\mu_r \approx 1/\pi\eta a^3$ [10]. The hydrodynamic coupling of rotation and translation between two spheres, the so-called *rotlet* effect [10], decays fast in space ($\sim 1/r^2$) and is neglected, similar to previous studies [5]. Rotlet corrections are examined separately [11]. The vectorial random displacements $\boldsymbol{\xi}(t)$ and $\Xi(t)$ model the coupling to a heat bath and obey the fluctuation-dissipation relations $\langle \boldsymbol{\xi}_i(t)\boldsymbol{\xi}_j(t') \rangle = 2k_B T \boldsymbol{\mu}_{ij} \delta(t-t')$, $\langle \Xi_i(t)\Xi_j(t') \rangle = 2k_B T \mu_r \delta_{ij} \delta(t-t')$ and $\langle \Xi_i(t)\boldsymbol{\xi}_j(t') \rangle = \mathbf{0}$, which are numerically implemented by a Cholesky factorization [9].

For the numerical integrations we discretize Eqs. (2) and (3) with a time step Δ and rescale all lengths, times and energies, leading to the dimensionless parameters $\tilde{\Delta} = \Delta k_B T \mu_0 / a^2$, $\tilde{\mu}_r = \mu_r a^2 / \mu_0 = 3$, $L_p/L = A/(a N k_B T)$ and $\tilde{\omega} = \omega a^2 / (\mu_0 k_B T)$. We set the twist-bend rigidity ratio to $C/A = 2$. This choice, which corresponds to a negative Poisson ratio $\sigma = A/C - 1$ [4], is relevant for typical biopolymers [12, 13]. We also studied the $C/A = 1$ case, with no qualitative difference [11]. For sufficient numerical accuracy we choose time steps in the range $\tilde{\Delta} = 10^{-4}$ - 10^{-7} . Output values are calculated every 10^3 - 10^4 steps, total simulation times are 10^6 - 10^8 steps. Clamped boundary conditions at the forced end, i.e. $\partial_s \mathbf{r}(0) = 0$, are realized by fixing the first two monomers in space by applying virtual forces, which also act (via the mobility tensor) on the rest of the filament. A mobile filament is obtained by switching off the virtual forces along the axis (chosen as the $\hat{\mathbf{x}}$ direction). The rotational driving at the base imposes $\dot{\theta}_1(t) = \omega$. Force- and torque-free boundary conditions are adopted for the other end. As initial shape of the filament we take circular sections specified by the angle α ; see the inset of fig. 1 (g). The straight rod configuration thus corresponds to $\alpha = 0$. The number of beads is in the range $L/a = N = 20 - 40$.

At low rotational frequency, $\omega < \omega_c$, the rod is twisted but remains straight and the torque at the base balances the total rotational drag, $\mu_r^{-1}\omega L \sim C\Omega_3(0)$. On the scaling level, the rod buckles when the twisting torque $C\Omega_3(0)$ becomes comparable to the bending torque, A/L , giving a critical frequency $\omega_c \sim \mu_r A/L^2$ independent of the twist rigidity C . The asymptotically exact linear analysis based on slender-body hydrodynamics predicts a critical frequency [5]

$$\omega_c \cong 8.9\mu_r A/L^2 = 8.9\mu_r k_B T (L_p/L)^2 / L_p. \quad (4)$$

The time evolution of the rod shape for $N = 30$, persistence length $L_p/L = 10^3$ for $\omega/\omega_c = 1.20$ (starting with a straight shape $\alpha = 0$) is shown in fig. 1a. Twirling is unstable against thermal disturbance and the filament buckles to relieve twist, leading to crankshafting motion. As will be discussed in more detail below, the radial distance of the free end from the rotational axis, called R , initially increases exponentially in time until the filament bends over (see fig. 1b) and the steady overwhirling shape is reached. Overwhirling is a combination of rigid-body-like rotation with frequency χ and axial spinning. The crankshafting frequency χ increases drastically across the kinetic transformation state, while the torque applied at the base, M , shows a small but steep decrease (see fig. 1c-d); in other words, the transition to the whirling state can be viewed as a way to reduce the dissipated power. In figs. 1e-1 and e-2 the steady state values of χ and M are plotted against ω/ω_c across the transition for a rather stiff rod with $L_p/L = 10^3$. A pronounced hysteresis is revealed, suggesting that the observed transition is strongly discontinuous and the final state depends not only on the driving frequency ω but also on the initial shape of the filament (described by α). This stands in vivid contrast to the analytics predicting a continuous transformation [5]. The bifurcation frequencies depend on

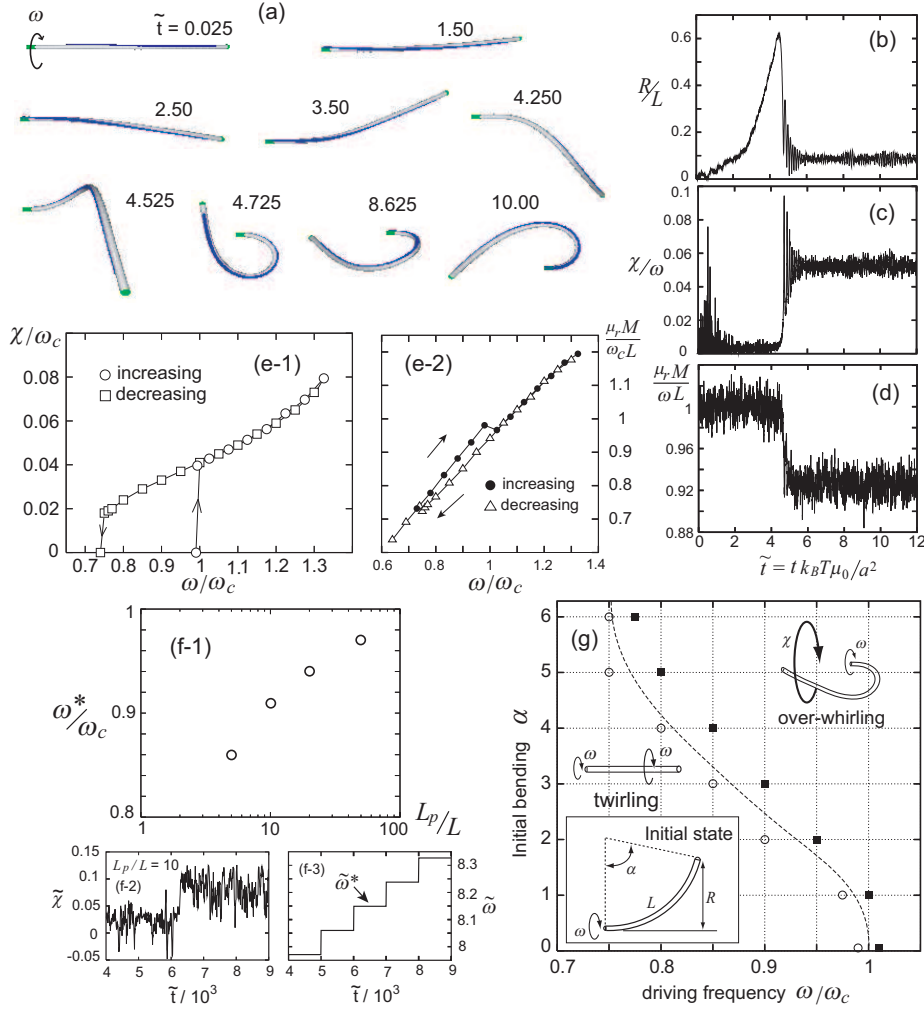


Fig. 1 – (a) Sequence of snapshots of a rotating filament of length $N = 30$ and stiffness $L_p/L = 10^3$ for $\omega/\omega_c = 1.20$. Corresponding time evolutions of (b) the end-point radius R , (c) the cranksafting frequency χ and (d) the torque applied at the driving end M . (e-1) Hysteresis loop of χ for a $N = 30$ and $L_p/L = 10^3$ rod. (e-2) same for M . (f-1) Observed transition frequency ω^* for varying stiffness L_p/L for $N = 30$ rod. (f-2 and f-3) Corresponding time series of χ and ω close to the transition for $L_p/L = 10$. (g) Zero-temperature stability diagram as a function of initial bending angle α and driving frequency ω for a $N = 30$ rod. All data are for an immobile filament.

the rate with which the frequency is changed, but only for very flexible rods does the hysteresis disappear. We construct the stability diagram shown in fig. 1 (g) in the (ω, α) plane at zero temperature (i.e. the deterministic noise-less limit where $L_p/L = \infty$) by following the time evolution of a rod with an initial circular shape with bending angle α and the stationary twist profile. Twirling is the final stationary state for a filament with an initial shape bending angle below the separatrix, while above the separatrix the overwhirling state is obtained. The separatrix terminates for $\alpha = 0$ at $\omega = \omega_c$ as given by eq. (4) [5], indicating that ω_c is an instability point and actually the correct critical frequency at zero-temperature above

which the filament is unstable against infinitesimal disturbance. By construction, the stability diagram does not depend on the stiffness of the filament. The cause of the discrepancy to the previous simulation [6] at zero temperatures which yielded a much lower transition frequency is unclear.

At finite temperature (i.e. finite L_p/L), the overwhirling transition is observed below ω_c : In fig. 1 (f-1) the transition frequency ω^* is plotted as a function of L_p/L , obtained from simulations where the driving frequency ω is increased in steps of size $\Delta\omega = \omega_c/100$ every 10^7 simulation time steps. The time-dependent behavior of χ and ω across the transition is plotted in fig. 1 (f-2) and (f-3), respectively, for $L_p/L = 10$, from which ω^* is determined. An even slower frequency increase rate gives a slightly lower ω^* , so the results in fig. 1 (f-1) correspond to an upper limit of the transition in the stationary limit. A simple scaling arguments explains the observed trend: Balancing the bending energy $E \sim A\alpha^2/(2L)$ with $k_B T/2$, one obtains a spontaneous mean squared bending angle $\langle\alpha^2\rangle \sim L/L_p$, which is larger for smaller L_p and thus leads to reduced stability (see the stability diagram). Below $L_p/L \sim 5$, the filament switches frequently between the two states, and the transition is washed out. The dependence of the twirling-overwhirling transition on the persistence length could be experimentally tested with actin or tubulin filaments of varying length.

For a stiff rod and short times, we expect universal shape dynamics for frequencies slightly above ω_c . Consider a small amplitude whirling motion ($R/L \ll 1$) at cranksafting frequency χ for supercritical frequency $\varepsilon \equiv (\omega - \omega_c)/\omega_c > 0$. As we will show, the small amplitude whirling is unstable for any ε , but lasts for a long time for small enough ε due to critical slowing down. The rod shape is approximated as $\mathbf{r}(s) \approx s\hat{\mathbf{x}} + \mathbf{r}_\perp(s)$, and $\dot{\mathbf{r}}(s) = \chi\hat{\mathbf{x}} \times \mathbf{r}_\perp(s)$ for cranksafting. Since χ grows much more slowly in time than the end-point radius R , it can be estimated by assuming that the transverse drag force per length, $\chi|\mathbf{r}_\perp|/\mu_0$, is roughly equal to the bending force per length, $A|\mathbf{r}_\perp|/L^4$, giving $\chi \sim A\mu_0/L^4 \sim (a/2L)^2\omega_c$. After a short time transient, the twist density Ω_3 has built up the stationary linear profile, $\Omega_3 = \omega/\mu_r C(s - L)$, and thereby reached $\dot{\Omega}_3 = 0$. The difference in rotational velocities about the local tangents at $s = 0$ and $s = L$, $\Delta\omega$, satisfies $-\Delta\omega = \chi[1 - \hat{\mathbf{x}} \cdot \mathbf{t}(L)]$ (for a derivation see ref. [5]). Considering the local balances of viscous and elastic twisting torques $\mu_r^{-1}\omega L \sim C\Omega_3$ at $s = 0$ and $s = L$, we see that the net torque $\Delta M \sim \mu_r^{-1}\Delta\omega L$ must contribute to the whirling motion of the filament. On the other hand, the elastic energy E of the rod with the amplitude R is estimated to be $E \sim 2AR^2/L^3$, while the power dissipation P_d by the rigid-body like rotation is $P_d \sim v^2 L/3\mu_0 = \chi^2 R^2 L/3\mu_0$, where $v = \chi R$ is the rotational velocity. The power balance condition, according to which the sum of the change of the elastic energy per unit time and the hydrodynamic rigid-body dissipation balances the net torque injected into the rod per unit time, implies $\dot{E} + P_d \sim \omega \Delta M$. Note that the remaining power input $\omega(M - \Delta M)$ is independently balanced with the dissipation by axial rotation. Approximating $1 - \hat{\mathbf{x}} \cdot \mathbf{t}(L) \approx 2R^2/L^2$ we finally arrive at $\dot{R}(t) \sim \varepsilon \chi R(t)$. The end point radius $R(t)$ thus evolves exponentially in time for $\varepsilon > 0$, and the growth rate $\Gamma(\omega) = d(\log R)/dt$ satisfies the linear relation $\Gamma/\chi \sim (\omega - \omega_c)/\omega_c$. In fig. 2 (a), the numerically obtained Γ/χ , which is almost constant while $R/L \ll 1$, is plotted as a function of the supercriticality $\varepsilon = (\omega - \omega_c)/\omega_c$ for filaments of various length and stiffness. The thermal noise is switched off for improved data accuracy. The data scale linearly for small ε in agreement with the prediction (with a numerical prefactor of the order of unity), verifying the validity of the arguments and approximations presented above. For larger ε , nonlinearity comes in, leading to deviations from the simple linear law. For the numerical calculations the presence of this critical slowing down can be a problem because stationary states are only obtained after a long waiting time.

In the case when the filament is allowed to move along the axis of rotation, a finite average velocity is observed in the overwhirling regime: the filament is propelled due to the formation

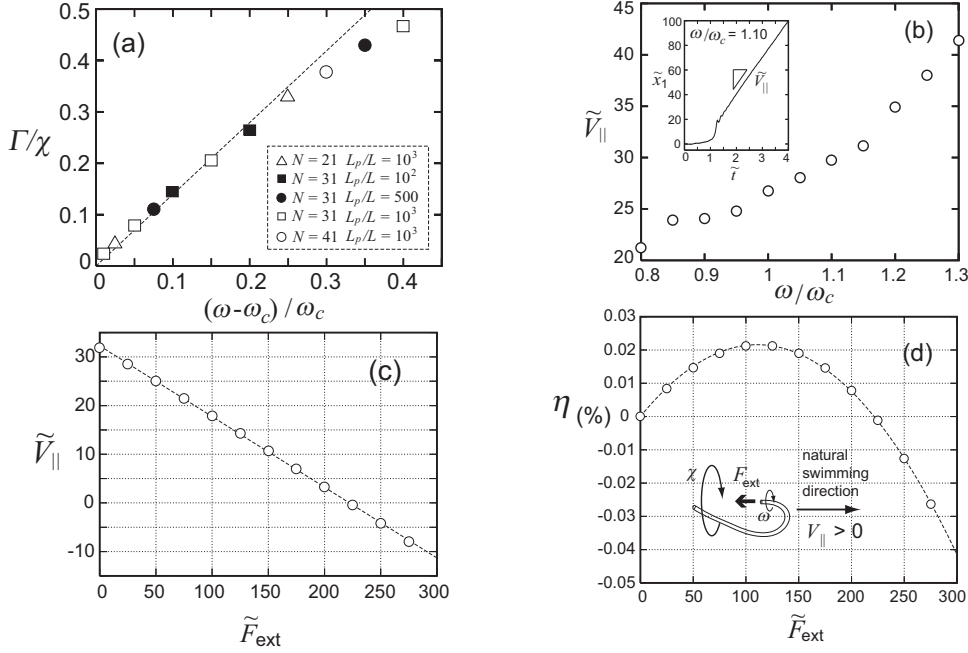


Fig. 2 – (a) Growth rate of end radius Γ divided by the crankshafting frequency χ as a function of the supercriticality parameter $\varepsilon = (\omega - \omega_c)/\omega_c$ for rods with various length and stiffness obtained in the noise-less limit. (b) Rescaled propulsion velocity along the rotation axis $\tilde{V}_{||} = V_{||}a/\mu_0k_BT$ in the overwhirling state, plotted against ω/ω_c (Inset: actual time evolution of the base position \tilde{x}_1 across the shape transition for $\varepsilon = 0.1$). (c) $V_{||}$ versus the rescaled external force $\tilde{F}_{ext} = aF_{ext}/k_BT$ for $\varepsilon = 0.1$. (d) Efficiency η as a function of \tilde{F}_{ext} with the parabolic fit (dashed line). All data in (b)-(d) are for $N = 30$ and $L_p/L = 10^3$ (i.e. at finite temperature).

of a helical shape which breaks the time-reversal symmetry of the problem. Accordingly, a jump in the propulsion velocity along the rotation axis $V_{||}$ is observed across the overwhirling transition, resulting in a drastically amplified forward thrust of the filament (see the inset of fig. 2 (b)). The propulsion velocity $V_{||}$ in the overwhirling regime is plotted in fig. 2 (b) as a function of ω/ω_c . Note that the overwhirling state is metastable for a wide range of frequencies below ω^* and thus the velocity is non-zero. The non-monotonic increase of $V_{||}$ with ω implies a complicated shape change of the rod as a function of ω . To study the swimming efficiency of this self-propelling object, we apply an external force F_{ext} at the filament base. The power converter efficiency is the ratio of the propulsive power output and the rotary power input, $\eta = F_{ext}V_{||}/(M\omega)$, where a positive F_{ext} is defined such as to work against the natural propulsion direction of the filament. The rotational and translational mobilities of the whole filament are defined by $\omega = \mu_{rr}M + \mu_{rt}F_{ext}$ and $V_{||} = \mu_{tr}M + \mu_{tt}F_{ext}$ [14]. Although for perfectly stiff propellers the mobility matrix is constant and symmetrical (i.e., $\mu_{rt} = \mu_{tr}$), due to the flexibility of the filament, the symmetry here is broken and the mobilities depend on the external torque M and force F_{ext} in a complicated non-linear manner. In the simulation, a substantial forward thrust is observed independent of the rotation direction, which suggests that μ_{tr} changes its sign when the torque N is reversed, similar to results obtained for a rod with vanishing twist rigidity that rotates on the surface of a cone [15]. $V_{||}$ varies linearly with F_{ext} as shown in fig. 2 (c), which means that μ_{tt} is independent of the

external force F_{ext} . Neglecting μ_{rt} , which is actually vanishingly small, while keeping μ_{tr} , we obtain $\eta = (\mu_{rr}\mu_{tt}F_{ext}^2 + \mu_{tr}\omega F_{ext})/\omega^2$, indicating that the efficiency becomes parabolic as a function of the external force. Figure 2 (d) shows the numerical data of η with the parabolic fit for $\varepsilon = 0.1$, which describes the data quite nicely. The highest efficiency is only of the order of 0.01%, which means that this self-propelling filament is quite inefficient compared to other known examples involving helices and other chiral objects [15], since most of the input power is dissipated by the axial spinning.

In summary, the elastohydrodynamics of a spinning filament in viscous fluid is studied by simulations including full coupling between elastic, thermal and hydrodynamic effects. Quantitative agreement with the analytically predicted critical frequency is obtained [5] in the absence of thermal fluctuations, in contrast to numerical simulations of the same problem [6]. We give evidence for the discontinuous nature of the twirling-overwhirling transition, in qualitative agreement with previous numerical works at zero temperature [6] but in contradiction to the analytical theory which might have to do with the neglect of non-linear effects [5]. Thermal fluctuations play a significant role in the transition behavior of a filament and lead to a decrease of the critical frequency in a range of filament stiffnesses L_p/L that is relevant to biopolymers. The parametrization proposed in this paper is entirely based upon a local-form description and advantageous for numerical implementations. Our dynamic simulation method is easily generalizable to other geometries such as rings or helices. A number of intriguing problems have to do with pulling on flexible nanospring [16] or buckling of twisted rods [1, 12]. Of particular biological interest is a spinning helical filament. Taking, for example, a diameter value of $a \approx 20$ nm and a typical stiffness $L_p/L \approx 10^3$ of a bacterial flagellum at physiological conditions [17], we find $\omega_c \sim 10^3$ s $^{-1}$ in water with the viscosity $\eta \sim 10^{-3}$ Pa-s, which is easily achievable in laboratory experiments. Details on the interplay of thermal fluctuations and shape instabilities will be reported elsewhere [11].

We thank M. Manghi for valuable discussions and the program for Research Abroad of the Japan Society for the Promotion of Science (JSPS) and the German Science Foundation (DFG, SPP1164) for financial support.

REFERENCES

- [1] GORIELY A. and TABOR M., *Nonlinear Dynamics*, **21** (2000) 101 and references therein.
- [2] WIGGINS C. H., *Math. Meth. Appl. Sci.*, **24** (2001) 1325.
- [3] KÄS J., STREY H., BÄRMANN M. and SACKMANN E., *Europhys. Lett.*, **21** (1993) 865.
- [4] LANDAU L. D. and LIFSHITZ E. M., *Theory of Elasticity* (Pergamon Press, Oxford) 1980.
- [5] WOLGEMUTH C. W., POWERS T. R., and GOLDSTEIN R. E., *Phys. Rev. Lett.*, **84** (2000) 1623.
- [6] LIM S. and PESKIN C. S., *SIAM J. Sci. Comput.*, **25** (2004) 2066.
- [7] GOLDSTEIN R. E., POWERS T. R., and WIGGINS C. H., *Phys. Rev. Lett.*, **80** (1998) 5232.
- [8] ALLISON S., AUSTIN R., and HOGAN M., *J. Chem. Phys.*, **90** (1989) 3843.
- [9] ERMAK D. L. and MCCAMMON J. A., *J. Chem. Phys.*, **69** (1978) 1352.
- [10] HAPPEL J. and BRENNER H., *Low Reynolds Number Hydrodynamics* (Noordhoff, Leyden) 1973.
- [11] WADA H. and NETZ R. R., in preparation.
- [12] VOLOGODSKII A. V., and MARKO J. F., *Biophys. J.*, **73** (1997) 123.
- [13] TSUDA Y., YASHUTAKE H., ISHIJIMA A., and YANAGIDA T., *Proc. Natl. Acad. Sci. U.S.A.*, **93** (1996) 12937.
- [14] PURCELL E. M., *Proc. Natl. Acad. Sci. U.S.A.*, **94** (1997) 11307.
- [15] MANGHI M., SCHLAGBERGER X., and NETZ R. R., *Phys. Rev. Lett.*, **96** (2006) 068101.
- [16] SMITH B., ZASTAVKER Y. V. and BENEDEK G. B., *Phys. Rev. Lett.*, **87** (2001) 278101.
- [17] TURNER L., RYU W. S., and BERG H. C., *J. Bacteriol.*, **182** (2000) 2793.